Preprints are preliminary reports that have not undergone peer review.
They should not be considered conclusive, used to inform clinical practice,
or referenced by the media as validated information.

Dissipationless zero energy epigraphene edge state for nanoelectronics

Vladimir Prudkovskiy
IEMN CNRS https://orcid.org/0000-0003-4375-5561
Yiran Hu
Georgia INstitute of Technology
Kaimin Zhang
Tianjin University
Yue Hu
Georgia Institute of Technology
Peixuan Ji
Tianjin UNiversity
Grant Nunn
Georgia Institute of Technology
Jian Zhao
Tianjin University
Chengqian Shi
Tianjin University
Antonio Tejeda
Université Paris-Sud https://orcid.org/0000-0003-0125-4603
David Wander
CNRS
Alessandro de Cecco
CNRS
Clemens Winkelmann
Institut Neel https://orcid.org/0000-0003-4320-994X
Yuxuan Jiang
National High Magnetic Field Laboratory
Tianhao Zhao
Georgia Institute of Technology
Katsunori Wakabayashi
Kwansei Gakuin University https://orcid.org/0000-0002-9147-9939
Zhigang Jiang
Georgia Institute of Technology https://orcid.org/0000-0001-9884-3337
Lei Ma

Tianjin University
Claire Berger
CNRS- Georgia Tech International Research Lab 2859
Walt de Heer (deheer.walt@gmail.com)
Georgia Institute of Technology

Article

Keywords: Deposited Graphene, Plasma-based Lithography, Hall Effect, Zero-energy Fermion, Quantum Computing

Posted Date: May 7th, 2021

DOI: https://doi.org/10.21203/rs.3.rs-492561/v1

License: This work is licensed under a Creative Commons Attribution 4.0 International License.
Read Full License

Dissipationless zero energy epigraphene edge state for nanoelectronics

*Vladimir S. Prudkovskiy[1, 2, 3], Yiran Hu[2], Kaimin Zhang[1], Yue Hu[2], Peixuan Ji[1], Grant Nunn[2], Jian Zhao[1], Chenqian Shi[1], Antonio Tejeda[4, 5], David Wander[3], Alessandro De Cecco[3], Clemens B. Winkelmann[3], Yuxuan Jiang[6], Tianhao Zhao[2], Katsunori Wakabayashi[7, 8], Zhigang Jiang[2], Lei Ma[1, 9, †], Claire Berger[2, 3, 10], Walt A. de Heer[1, 2, *]*

[1] Tianjin International Center for Nanoparticles and Nanosystems, (TICNN) Tianjin University, 92 Weijin Road, Nankai District, China, 300072

[2] School of Physics, Georgia Institute of Technology, Atlanta, Georgia 30332, United States

[3] Institut Néel, Univ. Grenoble Alpes, CNRS, Grenoble INP, 38000 Grenoble, France

[4] Laboratoire de Physique des Solides, CNRS, Univ. Paris-Sud, 91405 Orsay, France

[5] Synchrotron SOLEIL, L'Orme des Merisiers, Saint-Aubin, 91192 Gif sur Yvette, France

[6] National High Magnetic Field Laboratory, Tallahassee, Florida 32310, United States

[7] School of Science and Technology, Kwansei Gakuin University, Gakuen 2-1, Sanda 669-1337, Japan

[8] Center for Spintronics Research Network (CSRN), Osaka University, Toyonaka 560-8531, Japan

[9] State Key Laboratory of Precision Measurement Technology and Instruments, Tianjin University, 92 Weijin Road, Nankai District, China, 300072

[10] International Research Lab 2958, Georgia Tech-CNRS, 57070 Metz, France

Corresponding authors

*e-mail: walter.deheer@physics.gatech.edu

† e-mail maleixinjiang@tju.edu.cn

Abstract:

The graphene edge state is essential for graphene electronics and fundamental in graphene theory, however it is not observed in deposited graphene. Here we report the discovery of the epigraphene edge state (EGES) in conventionally patterned epigraphene using plasma-based lithography that stabilizes and passivates the edges probably by fusing the graphene edges to the non-polar silicon carbide substrate, as expected. Transport involves a single, essentially dissipationless conductance channel at zero energy up to room temperature. The Fermi level is pinned at zero energy. The EGES does not generate a Hall voltage and the usual quantum Hall effect is observed only after subtraction of the EGES current. EGES transport is highly protected and apparently mediated by an unconventional zero-energy fermion that is half electron and half hole. Interconnected networks involving only the EGES can be patterned, opening the door to a new graphene nanoelectronics paradigm that is relevant for quantum computing.

The predicted properties of deposited quasi-freestanding graphene were so spectacular that it was expected to imminently trigger a graphene nanoelectronics revolution[1]. However the edges of lithographically patterned deposited graphene are invariably insulating due to uncontrollable chemical and structural disorder[2-6]. Since the edge state dominates transport in all neutral graphene nanostructures,[7-15] few, if any of the predictions could be tested experimentally. More importantly, the inability to stabilize patterned graphene edges[4-6] derailed the ambitious graphene nanoelectronics effort replacing it with much more modest goals.[16,17]

Evidence of the protected graphene edge state[7-9,12-14] (not to be confused with quantum Hall edge states [14,18-24]) was first found in 40 nm wide self-assembled graphene ribbons that form[25] on the high temperature annealed sidewalls of steps etched on the polar faces of electronics grade hexagonal SiC.[26,27] Electron microscopy revealed that the sidewall ribbons terminated in the SiC, thereby stabilizing and passivating the edges.[28-30] Sidewall ribbons exhibit dissipationless (ballistic) transport over tens of microns, even at room temperature. Surprisingly, the conductance was found to be 1 G_0=1 e^2/h rather than the predicted 2 G_0[7,8,13-15] where e is the charge and h is Planck's constant. Unfortunately, the sidewall topology is unsuited for nanoelectronics. It is also incompatible with conventional magneto-transport measurement methods. Hence essentially none of the numerous edge state theories could be tested, which, as we show here, in fact fundamentally diverge from long-standing predictions.[13,14,24,31]

We subsequently produced SiC wafers that were cut along crystal faces corresponding to the annealed sidewall facets. The epigraphene is found to be charge neutral as required for nanoelectronics so that the Fermi energy E_F=0 (in contrast graphene monolayers grown on the commercial polar SiC faces have a charge density n≈10^{13} cm^{-2}, corresponding to a E_F of about 0.3 eV[32-36]). The conventionally patterned interconnected nanostructures exhibit 1 G_0 ballistic

conduction at zero magnetic field, up to room temperature, and independent of edge chirality. The mean free path (mfp) of the EGES is on the order of 10 μm up to room temperature, whereas the mfp of the bulk of the sample is on the order of 10 nm. This demonstrates an unexpected high degree of protection and stands in stark contrast with conventional patterned deposited graphene, where the opposite is true: micron scale bulk mfp's have been observed in boron nitride supported deposited graphene, however the edges are invariably insulating.[5]

Strikingly, the quantized epigraphene edge state currents do not generate a Hall voltage, contrary to conventional theory[24]. This causes an anomalous quantum Hall effect, and signals that the EGES transport involves fundamentally different physics than generally assumed for the graphene edge state.[13,14,24]

We use the simple tight-binding description of the edge state (Fig.1) as a convenient starting point for discussion,[7-9,14,15] which shows that the Fermi level should be pinned at $E_F=0$ at the edge, as experimentally confirmed here. A comprehensive analysis reveals quantized transport involving an unconventional fermion, that is neither an electron nor a hole, since, for a given current, these would produce equal and opposite Hall voltages. Hence, we propose that the novel fermion that mediates this zero-energy mode is most likely half electron and half hole. While this description applies to Majorana fermions[37] alternatives may exist.

The combination of essentially dissipationless single-channel transport at zero energy in conventionally nanopatterned graphene on a commercially available electronic single crystal SiC is a very large step towards realizing the envisioned epigraphene electronics paradigm shift,[38] using coherent tunneling devices and phase coherent interconnected structures that are relevant for quantum computing.

The neutral epigraphene edge state

Figure 1A shows the tight binding (TB) electronic subbands (electronic waveguide modes) in a charge neutral 700 nm wide zigzag graphene ribbon near the K point.[7,8,15,39] This band structure is generic for all graphene ribbons with chiral edges, excluding only perfect armchair ribbons, as predicted and observed.[12,40,41] The n=0 subband, i.e. the graphene edge state (GES), is special. It is composed of a flat band at E=0, that is narrowly confined to the physical edges of the ribbon. It evolves at the K and K' points into linear dispersing electron and hole bands that are delocalized over the entire ribbon. In neutral graphene, the hole bands are occupied and the electron bands are unoccupied. The predicted flatband is half-filled in neutral graphene and gives rise to a peak in the density of states (the 0-DOS peak, Fig. 1B) at the graphene charge neutrality point (CNP, i.e. the Dirac point at E=0). The 0-DOS peak is a robust feature of "graphene molecules"[42-44] and has been experimentally confirmed in general for chiral graphene ribbons (Ref. [40], Fig 2e, and Ref. [41]).

A positive gate voltage V_G applied to graphene induces charge density n_c (Fig. 1C) thereby shifting CNP by $\Delta E = \hbar c^* \sqrt{\pi n_c}$ below the Fermi level where $c^* \approx 10^6$ m/s. (The inverse happens for negative V_G). However, theoretically, the 0-DOS peak pins the Fermi level at E=0 by depleting charges near the edge [45], analogous to a Schottky barrier.[46] The resulting electric fields cause band bending of the edge-localized branch of the n=0 band. The delocalized bands on the other hand essentially rigidly shift down by ΔE. Transport in the n=0 subband is expected to involve both the edge-localized and 2D branches of the GES, i.e. where the Fermi level intercepts n=0 subband as indicated in Fig. 1C.

The TB approximation is an excellent starting point to describe the basic properties of graphene[7,8,13,24] but electron-electron interactions significantly modify the properties of the

flatband,[13,47-50] making the GES a topic of great theoretical interest[31,37,49-51]. While those interactions will typically broaden the 0-DOS peak, pinning (which is an electrostatic effect) is expected to survive, so that the Dirac point properties of the GES are accessible as long as the 0-DOS peak is not saturated.

The 0-DOS saturates when $n_c\delta a_0=1/3$ where n_c is the gate induced bulk charge denstiy, δ is the depletion region, which is a fraction the dielectric thickness, and a_0 is the C-C bond length[45]. Hence saturation is expected for $n_c>10^{13}$ cm^{-2} in our geometry, i.e. above our experimental range. Epigraphene grown on commercial SiC wafers is highly charged,[32-34,52] which can saturate the 0-DOS peak, so that the EGES is not seen there. The edges in BN/exfoliated graphene/BN heterostructures are heavily n-doped and distorted[5,6] and the GES is not observed.

Neutral epigraphene characterization

Epigraphene is ideally suited for graphene nanoelectronics.[38,53] The quasi-freestanding graphene that self-assembles on electronics-grade silicon carbide (SiC) wafers[32-36] by thermal annealing[54,55] is of very high quality graphene and crystallographically aligned with the SiC lattice with contamination free interfaces. (for a review, see Ref. [34])

Experiments on self-assembled 40 nm wide graphene nanoribbons, that spontaneously form on the recrystallized, thermally annealed, sloping sidewalls of trenches etched in commercial SiC wafers,[25] show them to be charge neutral[26,56,57]. At the TICNN institute, we produced wafers cut from commercial electronics grade 4H SiC stock to expose sidewall facets (i.e. 4H SiC $(1\bar{1}0n)$, $n\approx5$[28,56]). Neutral epigraphene (N-EG) is grown on these facets using standard confinement-controlled sublimation methods[55], and interrogated using a variety of surface probes (Fig. 2). In its initial stages of growth N-EG shows characteristic trapezoidal islands (Fig. 2A) that

ultimately coalesce into a continuous single film. Scanning tunneling microscopy (Fig. 2B) reveals the graphene's hexagonal lattice structure. High-resolution angle resolved photoemission spectroscopy (ARPES) shows the iconic graphene Dirac cones (Fig. 2D) verifying the epitaxial alignment of the graphene with the SiC crystal lattice.[34] The N-EG Fermi level is at the Dirac point, $E_F=0$, demonstrating that N-EG is intrinsically charge neutral as confirmed in scanning tunneling spectroscopy (STS), Fig. 2C. Low temperature infrared magneto-spectroscopy (Fig. 2E) shows the expected graphene Landau levels that disperse as $E_{LL} = sgn(N_{LL})c^*\sqrt{2|N_{LL}|e\hbar B}$, where N_{LL} is the Landau level index and B is the magnetic field, characteristic of monolayer graphene and with a Fermi velocity $c^*=1.0\times10^6$ m/s. Note that for $N_{LL}=0$, $E_{LL}=0$. Low energy electron diffraction (LEED) of N-EG shows typical graphene pattern (Supplementary Fig. S3).

Edge disorder in free-standing graphene is difficult to control, because the acene edge atoms (that in general produce states at E=0 in "graphene molecules") are reactive and prone to spontaneous reconstruction.[42,43] However, epigraphene is well adhered to the SiC, giving it significant mechanical, chemical and thermal stability,[58,59] while exhibiting essentially ideal graphene properties.[32-36] To inhibit edge distortions during fabrication, the N-EG is first coated with a 30 nm alumina film, securely embedding the graphene between alumina and silicon carbide that are both refractory materials. The sandwich is then etched through a patterned mask, 16 nm into the SiC (Fig. 3) using the inductive coupled plasma etching (ICP) technique.[60] Hence, like a nanoscale plasma welding torch, the high temperature plasma (ion temperatures can exceed 5000K) cuts through the alumina, graphene and silicon carbide. In the process C-C and Si-C bonds are formed,[61] which fuse the ribbon edges to the SiC, thereby producing stable neutral edges that terminate in the SiC, as occurs in the self-assembled ribbons that are annealed

at ≈1500°C.[26-29,55] The alumina coating, that is used as the top gate dielectric, greatly reduces the mobility of the graphene bulk, with mfp's <10 nm (Supplementary Fig. S7). However it does not affect the EGES with mfp's > 20 μm, leading to the observed vivid contrast between EGES transport and bulk transport.

Segmentation and branching of the EGES

Figure 4A (inset) shows a schematic diagram of the device. Transport measurements were performed at temperatures from T=2 K to T=300 K in magnetic fields up to |B|=9 T. Resistances are indicated by $R(V_G, B, T)_{ij,kl} = V_{kl}/I_{ij}$, where V_{kl} is the voltage measured between contacts k and l and I_{ij} is the applied current between contacts i and j. The longitudinal voltage is $V^L = (V(B)+V(-B))/2$, and the Hall voltage is $V^H=(V(B)-V(-B))$; R is measured in units of R_0 where $R_0=1/G_0=h/e^2\approx 25.8$ kΩ and conductances G are defined as 1/R. A gate voltage V_G induces a charge density n_c according to $V_G=1.16\times 10^{-7}\sqrt{n_c}+ 8.2\times 10^{-13}\, n_c$ where V_G is in volts and n_c in cm^{-2}. The first term represents the experimentally determined quantum capacitance (Supplementary Fig. S5). The device can be decomposed in segments labeled **A** to **H** that join at junctions, i.e. at the intersections of horizontal and vertical 700 nm wide ribbons (Fig. 4 inset). The vertical direction in Fig, 4 inset is approximately 5° away from the zigzag direction and the horizontal direction is approximately 5° from the armchair direction. We next show that the vertical and horizontal ribbon segments are ballistic single channel conductors at the charge neutrality point.

Figure 4A shows $R^L_{40,4X}$ (X=0, 1, 2, 3), corresponding to $R^L_{\mathbf{A+B+C+D}}$; $R^L_{\mathbf{B+C+D}}$; $R^L_{\mathbf{C+D}}$; $R^L_{\mathbf{D}}$ at T=4.5 K for perpendicular magnetic fields B ranging from 0 to 9 T. Figure 4B shows $R_{\mathbf{E}}=R^L_{11',10}$ and $R_{\mathbf{E+H}}=R_{11',11'}$ for several temperatures from T_i=2 K to 300 K, and for B=0 T and for a

perpendicular magnetic field B=9 T. Resistances (in units of R_0=h/e^2) measured at CNP closely equals the number of segments, so that the resistance per segment is very close to 1 R_0. Similarly, at CNP and B=9 T, R_E≈1 R_0, R_{E+H}≈ 2 R_0 for all temperatures studied. Hence, at CNP the resistance per segment is approximately 1 R_0 at all temperatures both for nearly zigzag and armchair segments.

Conductance quantization at CNP is already obvious at zero field and is enhanced in high field. Deviations from perfect quantization at zero field are due to weak localization at low temperatures and thermal broadening of the bulk states at high temperatures that are both overcome in a magnetic field (see below). Conductance reductions due to finite EGES mfp's are also relatively small. Away from CNP, the (low mobility) bulk increasingly participates in the transport.

The Landauer formulism treats the conductance as the sum of the contributions of the individual subbands shown in Fig. 1. The GES has the index n=0 and the bulk subbands have n≠0 indices. Hence, the conductance G of a graphene segment of length L and width W (for B=0) can be decomposed as[62]

$$G = G_{edge} + G_{bulk} \qquad \text{(Eq. 1)}$$

$$G_{edge} = G_0(\Theta_0^+ + \Theta_0^-)$$

$$G_{bulk} = \sum_{n\neq 0}\left(\frac{4G_0}{k_B T}\right)\int \Theta_n(E)\frac{exp(\alpha)}{(exp(\alpha)+1)^2}dE$$

Here α=(E-E_F)/k_BT, where the Fermi energy is $E_F = \hbar c^* \sqrt{\pi n_c}$ (e.g. E_F=35 meV for n_c=10^{11}/cm^2) and $\Theta_n(E)$ is the transmission coefficient of the nth subband. Following Ref. [48], we assume that only the majority spin band contributes so that we neglect $\Theta_0^-(E_F)$.

Segmentation is consistent with the Landauer picture near E=0, with ballistic ribbons and isotropic scattering of the EGES occurring at the junctions. In the junction, transport is not protected so that EGES charge carriers are scattered by the random impurity potentials; 1 R_0 per segment indicates $\Theta \approx ½$ implying that forward- and back-scattering are equally probable, as for self-assembled epigraphene ribbons provided with an invasive probe.[26]

Ignoring coherence effects, $G_{edge}=G_0.(1+L/\lambda_{edge})^{-1}$, where λ_{edge} is the mpf of the GES and the conductance of the nth subband is $G_n=4G_0.(1+L/\lambda_n)^{-1}$, so that for the bulk, $\Theta_n(E)=(1+L/\lambda_{bulk}(E))^{-1}$ for $E<E_n$ where $\lambda_{bulk}(E) =\lambda_n$ is the bulk mfp.[62]

Four-point conductance measurements of segments **B** and **C** (Supplementary Fig. S7) show that the bulk conductivity is $\sigma=n_e e\mu$ with a bulk mobility $\mu\approx750$ $cm^2V^{-1}s^{-1}$ for

$n_c>2\times10^{11}$ cm^{-2}, corresponding to λ_{bulk}=6.5 nm at $n_c=10^{12}$ $/cm^2$. For $|n_c|< 2\times10^{11}$ $/cm^2$, the mobility increases (Supplementary Fig. S7). The independence of the mobility on charge density for large n_c is typical for graphene[13,63,64] and indicates scattering from charged impurities (of both signs) with a density $|n_{imp}|\approx7\times10^{12}$ cm^{-2}(Ref. [63], Eq. 1), mostly from the dielectric, however the non-conventional SiC substrate facet may also play a role.

For a 700 nm wide ribbon, Eq. 1 predicts that for $T> E_1/k_B\approx 40$ K, the thermal population of the bulk subbands increases the conductance at CNP (E_F=0) with increasing temperature. This is shown in Fig. 5B where the conductance $G_{11',11'}$ (corresponding to segments **E** and **H** in series) at CNP is plotted for several temperatures from T=2 K to T=300 K. Using Eq.1, a good fit is found for λ_{bulk}=24 nm near CNP. A magnetic field introduces an energy gap due to Landau quantization: E_{LL1}/k_B=1300 K for B=9 T, so that the conductance increase with temperature is not observed at B=9 T even at high temperatures (Fig. 5B). The conductance increase is not seen,

nor expected from Eq.1 in 40 nm self-assembled ribbons[26] up to room temperature since E_{LL1}/k_B=600 K.

For each segment **X** we determine the mfp λ_X of the EGES at CNP, and at B>2 T to overcome weak localization effects in the junctions (discussed below). Consequently, for a segment of length L_X (see caption Fig. 4) $G_X=G_0/(1+L_X/\lambda_X)$,[62] giving λ_A=13 μm; λ_B =15 μm; λ_C =12 μm; λ_D>20 μm; λ_E>20 μm; λ_F=20 μm; λ_G=15 μm; λ_H>20 μm; λ_I >20 μm. Like for self-assembled ribbons[26], λ_X is more than 1000 times larger than the mean free path of the bulk (Sup Mat Fig. S7), even at room temperature.

Figure 6B shows the measured conductance of Segment **A** at CNP, therefore that of the EGES, as a function of magnetic field for several temperatures $T \leq E_1/k_B$. The conductance increases with increasing B and saturates at $G \approx 1\ G_0$ for $B \gtrsim 2$ T. The minimum conductance at B=0 increases non-linearly as a function of temperature (see also Supplementary Fig. S6). Similar behavior was observed in self-assembled ribbons with graphene leads,[26,27] but not in self-assembled ribbons with metal contacts.[26] This implies that the conductance decrease at low magnetic field and low temperature involves the graphene junctions, not the segments themselves nor the metal contacts. Wakabayashi[39] calculated the transmission of two graphene ribbons connected by a graphene junction in the Landauer-Büttiker formulism, and predicted that the transmission of the GES at E=0 in wide junctions is $\Theta \approx ½$, while $\Theta \approx 1$ in large magnetic fields. The increase is due to the suppression of coherent back scattering, i.e. the same mechanism that causes weak localization.[62,65]

The resistances on both sides of a ribbon segment are found to be identical, down to the fine structure (Supplementary Fig. S10), which implies that the EGES involves both physical edges

of the segment. This is expected for the GES (Supplementary Fig. S15) and precludes models where the edges are independent ballistic conductors.

Scattering on random impurities cause weak localization in the junction: in absence of a magnetic field at low temperatures, constructive interference increases back scattering, thereby reducing Θ. In a magnetic field and/or at high temperatures, constructive interference in the junction is suppressed[62] and we find that Θ increases to Θ=½ (as in the case of invasive probe on ribbons[26]).

Weak localization is suppressed when $B > B_c = h/e\lambda_\phi{}^2$, where $\lambda_\phi = \sqrt{c^*\lambda_{bulk}\tau_\phi/2}$ is the 2D coherence length and τ_ϕ is the coherence time.[65] Using the theoretical model of Ref. [66] for 2D, we find λ_ϕ≈40 nm (τ_ϕ=0.5 ps) (Fig. 6B), independent of T for T≤65 K. For comparison in Ref. [67] in 2D epigraphene on the SiC (0001)face, τ_ϕ is found to be ≈10 ps at T=4 K, and ≈1 ps at T=20 K, which extrapolates to 0.3 ps at T=65 K assuming a T^{-1} dependence as suggested in Ref. [67]. While the 3-parameter fits reproduce the data very well (Fig. 6B), 2D weak localization theory is not expected to be accurate for $k_BT<E_1$. This can explain why coherence times are consistent with Ref. [67] for T=65 K and not for lower temperatures.

The decoupled EGES

Figure 6A shows the longitudinal conductance of segment **A**: $G^L_{04,01}(V_G,B_i)=1/R^L_{04,01}$. At CNP, at B=9 T and T=4.5 K the conductance is reduced by 0.22 G_0 from 1 G_0. Since $G_\mathbf{A}=G_0/(1+L_\mathbf{A}/\lambda_\mathbf{A})$ and $L_\mathbf{A}$=3.6 μm, therefore λ_A=13 μm (See Supplementary Fig. S9 for T=40 K and 65 K). As the magnetic field decreases, the conductance further reduces by ΔG_{WL} due to the weak localization (WL) that is significant for B ≤2 T (Fig. 6B). Since weak localization is seen at CNP, it involves

the EGES current as it flows through the junction from one ribbon segment to the next. Note that the ΔG_{WL} reduction of the longitudinal conductance is observed for all V_G.

Important insight into the nature of the EGES is obtained by subtracting the conductance measured at CNP from all measurements. For B<2 T the resulting conductance, Fig. 6C, corresponds to $G_{bulk}= n_c e\mu W/L$ with μ=750 $cm^2V^{-1}s^{-1}$ as expected for segment A. This effect is also observed in self-assembled ribbons (Ref.[26], Fig. 4c-d). For B>2 T, at V_G=0.6V we observe a Shubnikov-de Haas (SdH) oscillation[68] associated with the N_{LL}=0 Landau level. Similar behavior is observed for T=40 K and 65 K (Supplementary Fig. S9), where the SdH amplitude is reduced,[68] quantitatively consistent with graphene.

We thus draw the important conclusion that the EGES conductance measured at CNP simply adds to the conductance of the bulk (see also Supplementary Fig. S8): $G^L(V_G, B_i)= G_{bulk}(V_G, B_i) + G^L(V_G=0, B_i)$. Since $G^L=I/V=(I_{edge}+I_{bulk})/V=G_{edge}+G_{bulk}$, then at V_G=0, $I=I_{edge}$. This analysis demonstrates that the EGES current does not depend on V_G.

Quantized *conductance* at CNP should not be confused with the disorder induced quasi-quantized *conductivity* that was believed to occur in exfoliated graphene flakes[1,69]. The later manifests as a rounding of $G(V_G)$ at CNP and the conductance is not quantized.

Hall measurements of the junction of segments **A** and **B**, $R_{Hall}=R_{04,11'}$, exhibit a plateau near $R_{Hall}\approx 0.25\ R_0$ (Fig. 6D) that is observed up to T=150 K (Fig. 5A), which is unusual, since the monolayer Hall plateau $R_{Hall}=½\ R_0$ and a bilayer is ruled out (Supplementary Fig. S1). Similar behavior is observed for the other two junctions. Non-quantized pseudo-plateaus are observed for $0<V_G<0.5$ V, as shown in Fig. 6E at several representative V_G indicated by arrows in Fig. 6D, whereas in this region $R^L=1/G^L \approx 1\ R_0$. These anomalies are not observed in graphene Hall bars without a GES.[19,35,36,70,71] We next show that the EGES causes the anomalies.

Note that $R_{Hall}=V_{Hall}/I=V_{Hall}/(I_{edge}+I_{bulk})$. Applying the same procedure as used above for the longitudinal conductance, we subtract the EGES current measured at CNP (i.e. at $V_G=0$) from the total current at any V_G to determine the bulk current. Specifically,

$I_{edge}(V_G=0, B)=V^L(V_G=0, B)/ R^L(V_G=0, B)$ so that

$$R^H_{bulk}(V_G,B) = \frac{V^H(V_G,B)}{I_{bulk}} = R^H_{meas}(V_G,B)\left(1-\frac{R^L(V_G,B)}{R^L(V_G=0,B)}\right)^{-1} \quad \text{(Eq.2)}$$

Figure 6F shows that this straightforward procedure (using only measured quantities) transforms the anomalous pseudo-plateaus including the 0.25 R_0 plateau, into a remarkably well defined, conventional ½ R_0 monolayer graphene quantum Hall plateau that starts close to the Dirac point (E≈15 meV). Moreover, in the classical regime (low B, high n_c), the expected (diffusive) 2D Hall effect is observed: $R_H=B/n_ce$ beyond the Hall plateaus (see also Supplementary Fig. S5).

Pinning and vanishing Hall voltage

The insensitivity of the EGES current to the gate voltage demonstrates that EGES is pinned at CNP as theoretically expected (Fig. 1C). Consequently, $E_F=0$ along the entire edge as long as the 0-DOS peak is unfilled (i.e. for $|n_c|<3\times10^{13}/cm^2$; $|V_G|<30$ V). From Fig. 1C we infer that the conductance-decoupled EGES corresponds with the edge localized branch of the n=0 subband at E=0. Pinning is expected in general in for chiral edges in general since they include acene edge atoms that contribute to the 0-DOS.[42,43] Note that related Fermi level pinning at the Dirac point has previously been observed in multilayer epigraphene.[72]

The increase in the conductance and of the Hall voltage with increasing V_G results from the contribution from the bulk as experimentally shown above, and is consistent with Fig. 1C. The delocalized branch of the n=0 subband is probably responsible for the observed increased mobility at CNP (Supplementary Fig. S7). Moreover, Fig. 1C also explains conductance

decoupling since the EGES is confined to the edges where the bulk bands and the delocalized n=0 band are delocalized over the entire ribbon, so that the overlap with the EGES is negligible (the quantum Hall regime requires more careful examination).

The polarity of the Hall voltage indicates the polarity of the charge carriers[46], hence the vanishing of the Hall effect at CNP indicates that the transport involves equal electron and hole contributions, as in a perfectly compensated semimetal [73]. However in a semimetal (at least) two subbands must be involved, which is not expected in graphene and is inconsistent with the observed single 1 G_0 conductance. Positive and negative charge puddles could be perfectly balanced at CNP, but it is inconceivable that this delicate balance can be maintained independent of V_G.

Single channel ballistic EGES has now been observed in three distinct systems: narrow curved sidewall natural steps in SiC;[26,27] 40 nm graphene ribbons on annealed etched sidewall steps in SiC[26,27] and lithographically patterned N-EG graphene ribbons here, along approximately armchair and approximately zigzag directions. Moreover conductance quantization, and the absence of rounding of $G(V_G)$ near CNP (Fig. 6A and Supplementary Fig. S8g) are inconsistent with significant charge inhomogeneity (see also [74]). Hence, the combination of single channel ballistic transport and a vanishing Hall voltage is enigmatic.

We can now confidently assert that EGES properties derive from the pinned flatband at the edge, at E=0. Hence the EGES is pinned at the Dirac point singularity where the hole bands and electron bands meet.[14] Interactions within the flatband will ultimately determine its electronic structure and hence its transport properties. They will also broaden the 0-DOS peak but not significantly affect its area, so that pinning will not be significantly affected. Irrespective of the mechanism and independent of any model, the experimental transport measurements indicate

that transport in the EGES is at E=0 and mediated by a spin ½ fermion, to account for both the $1\ G_0$ transport, that is highly immune to scattering, and the absence of a Hall voltage. In a semimetal (which neutral graphene actually is[14]) transport is mediated by both electrons and holes. Hence a “semimetallic” quasiparticle can be envisioned as a forward moving electron and a backward moving hole that each transport ½ e of charge, consistent with the properties that we observe. Theoretically an example of such a fermion (i.e. a Majorana fermion) is predicted in graphene,[37] where contact with a superconductor provides the required mixing of the electron and hole bands at the Dirac point. We speculate that in our case, the metallic contacts and/or the bonding the substrate, may play a similar role. In addition, the substrate mechanically and chemically stabilizes the edges which does not occur in deposited graphene.

EGES networks are easily produced on N-EG substrates allowing the fundamental physical properties of this new intriguing, essentially unexplored new state to be investigated using conventional methods. It also allows interconnected EGES nanostructures to be studied to establish a foundation for epigraphene nanoelectronics using devices based on coherent tunneling across constrictions and gaps (Supplementary Fig. S13), spintronics (Supplementary Fig. S14) and coherent reflections (Supplementary Fig. S15).

Acknowledgements

Financial support was provided by the U. S. National Science Foundation-Division of Electrical, Communications and Cyber Systems (No 1506006) and NSF-Division of Material Research No 1308835. C.B, and V.P acknowledge funding from the European Union grant agreements No. 696656 and No 785219. This work was also made possible by the French American Cultural Exchange council through a Partner University Fund project. Financial support is acknowledged

from the National Natural Science Foundation of China (No 11774255), the Key Project of Natural Science Foundation of Tianjin City (No 17JCZDJC30100), and the Double First-Class Initiative of Tianjin University from the Department of Education in China. The magneto-infrared spectroscopy measurement was supported by the U.S. Department of Energy (grant No. DE-FG02-07ER46451) and performed at the National High Magnetic Field Laboratory, which is supported by NSF Cooperative Agreement No. DMR-1644779 and the State of Florida.
We thank Evangelos Papalazarou as well as François Bertrand and Patrick Lefebvre for their help with the ARPES measurement at the synchrotron Soleil-Cassiopée beam line.
Nikolay Cherkashin is thanked for polishing preliminary non-polar SiC chips, and Chao Huan for preliminary spin polarized transport experiments. WdH thanks M. Crommie, C. Delerue, P.N First, L. Levitov, G. Mele, E. Rossi and O. Yazyev for helpful discussions.

Authors' contributions

VP, CB, Yiran H, Yue H, GN, performed transport measurements (Figs. 4-6), graphene growth, sample characterization (Figs. 2A, F) and device patterning. LM, KZ, PJ, JZ and CS, fabricated and characterized non-polar face SiC wafers, performed graphene growth (Fig. 2B inset) and high resolution STM measurements (Fig. 2B inset); ZJ, YJ and TZ performed the IR spectroscopy (Fig. 2E). CB, VP, and AT performed the ARPES experiments (Fig. 2D); DW, AdC and CW performed STM and STS experiments (Fig. 2B, C). KW provided theoretical support and Supplementary Fig. S15. CB and WdH directed the Atlanta based experiments. LM and WdH directed the TICNN efforts. WdH is primarily responsible for the analysis and interpretation.

Competing interests: The authors declare no competing interests.

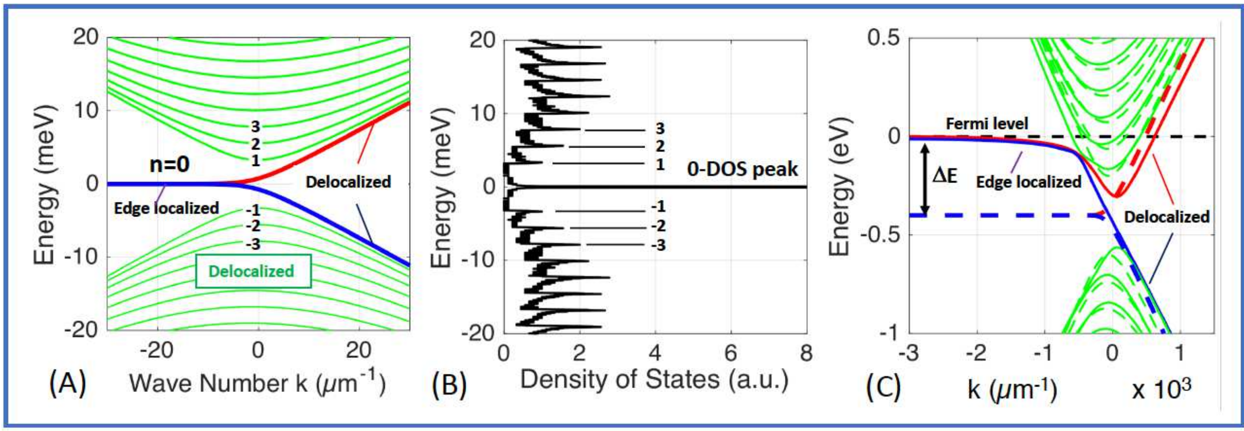

Figure 1. *Electronic structure of graphene ribbons*

(**A**) Tight-binding band structure of a neutral 700 nm wide graphene zigzag ribbon near the K point (k=0), that generically applies for all non-armchair ribbons[12]; CNP (i.e. the Dirac point) is at E=0. The GES (n=0) consists of a flat band localized at the physical edge that evolves into linearly dispersing electron and hole bands, delocalized over the whole ribbon. The bulk bands (n≠0) are delocalized and have vanishing amplitude at the edges. (**B**) The large density of states peak at E=0 (0-DOS peak) is due to the flatband. Subbands are separated by energy ΔE_n=2.4 meV; E_1= ΔE_1=3.3 meV, i.e. E_1/k_B=38 K. (For 40 nm wide self-assembled ribbons[26] E_1/k_B=660 K). (**C**) Tight-binding band structure for a 13 nm wide, gate charged graphene ribbon: $n_c=10^{13}$ cm^{-2}. The 0-DOS peak depletes charges near the edge, pinning E_F to 0. Dashed lines show that delocalized bands are essentially rigidly shifted by $\Delta E = \hbar c^* \sqrt{\pi n_c}$. Band-bending affects primarily the GES near, and to the left of the K point. Note that both the flatband and the dispersing n=0 subband intercept the Fermi level. For our 700 nm wide ribbons with V_G=1 V ($n_c \approx 10^{12}$ cm^{-2}) approximately 50 subbands are occupied and about 0.03 electrons per edge atom are absorbed in the 0-DOS peak (i.e. well below saturation that requires 0.33 electrons per edge atom).

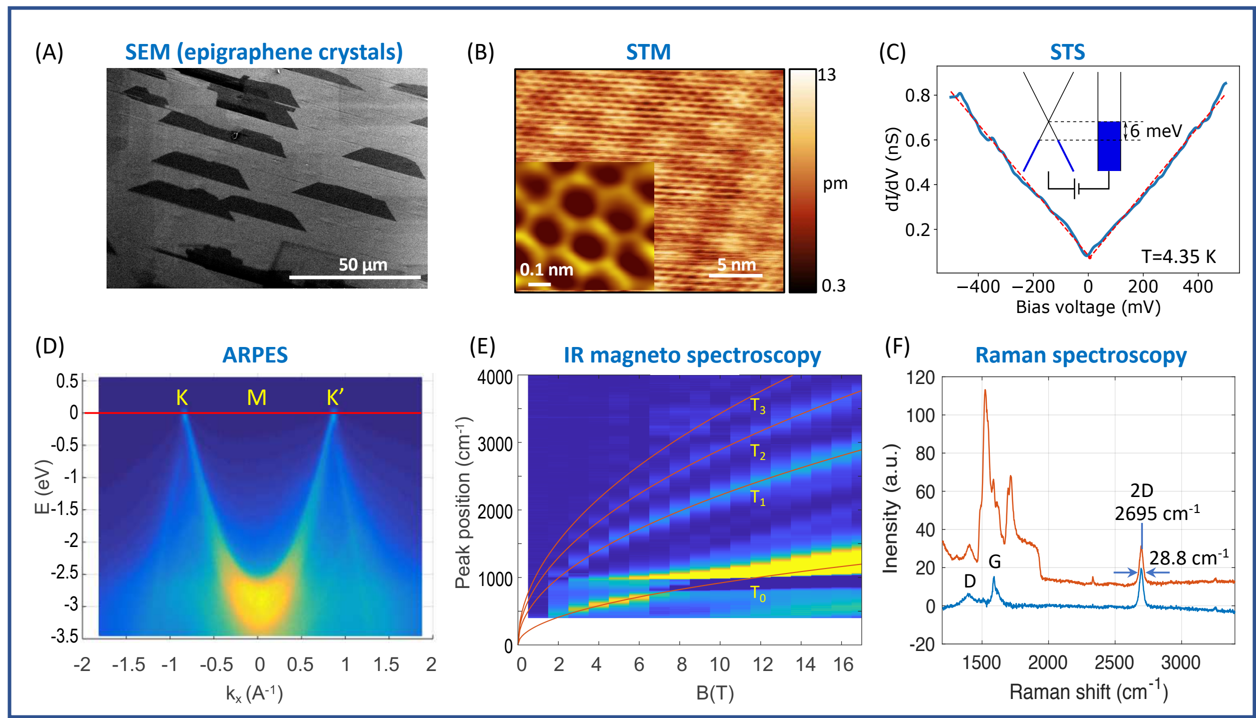

Figure 2. *Neutral epigraphene characterization.*

(A) SEM micrograph of trapezoidal graphene islands that form early in the growth and that coalesce to produce a uniform graphene coverage. **(B)** Low temperature STM image of the epigraphene; inset: characteristic hexagonal lattice of graphene. **(C)** Scanning tunneling spectrum (T=4.4 K; I_{set}=400 pA; V_{bias}=500 mV) revealing the graphene density of states with $|E_F\text{-}E_{CNP}|$<6 meV (inset) consistent with charge neutral graphene. Dashed line is a linear fit. **(D)** ARPES K-M-K' scan (beam energy 200 eV; E_F=197.4 eV; T=300 K) showing graphene Dirac cones with c^*=1.06x10^6 m/s and E_F=E_{CNP} confirming charge neutrality and no significant anisotropy (see also Fig. S3). **(E)** Infrared magneto-spectroscopy. Measured transitions $T_{0,1,2,3}$, follow monolayer graphene $\sqrt{B}$ dispersion (red lines). **(F)** Raman spectra. Raw spectrum (red) and after SiC spectrum subtraction (blue), showing the typical D, G and 2D graphene peaks. The 2D peak position and width (Lorentzian fit) correspond to monolayer graphene.[75]

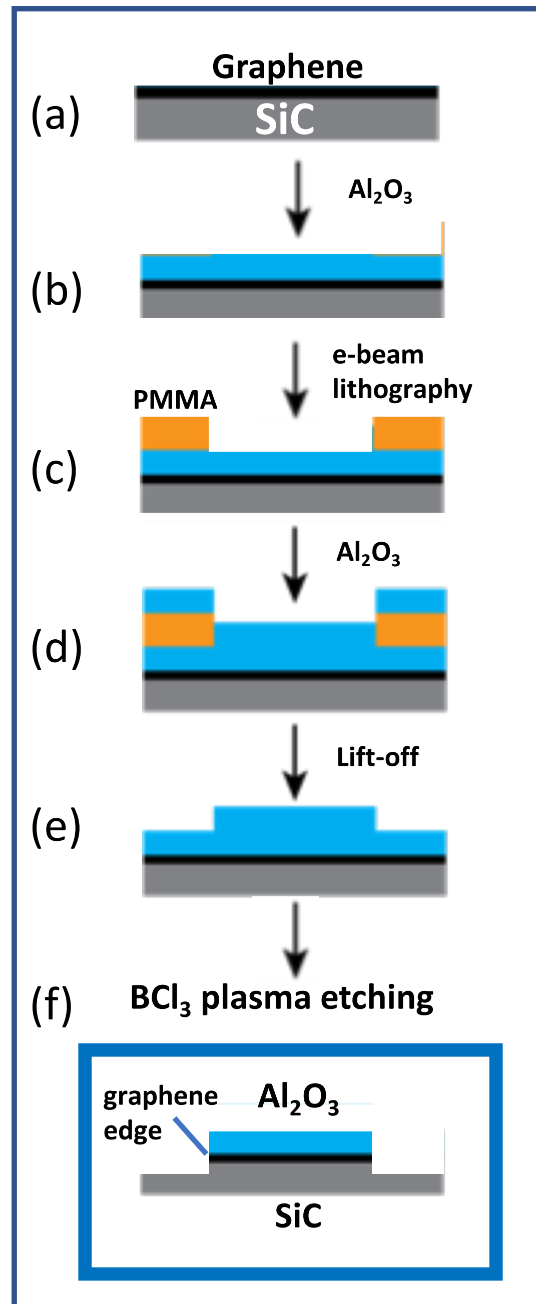

Figure 3. *Nanolithography process that ensures the integrity of the graphene edges.*

(a) High temperature annealing of N-EG at 1500°C preferentially evaporates silicon and the remaining carbon rich surface anneals to produce a high quality epigraphene monolayer.[55] **(b)** A 30 nm alumina layer is deposited, securely embedding the graphene between alumina and silicon carbide. **(c)** After development of e-beam patterned polymer mask. **(d)** Application of 20 nm of alumina. **(e)** After lift off the polymer mask. **(f)** A highly directional plasma (ICP) uniformly cuts through the alumina/graphene/SiC sandwich and 16 nm into the SiC. The high temperature (>5000°C) in the plasma vaporizes all of the materials in the sandwich and is expected to fuse the graphene edges to the SiC[61].

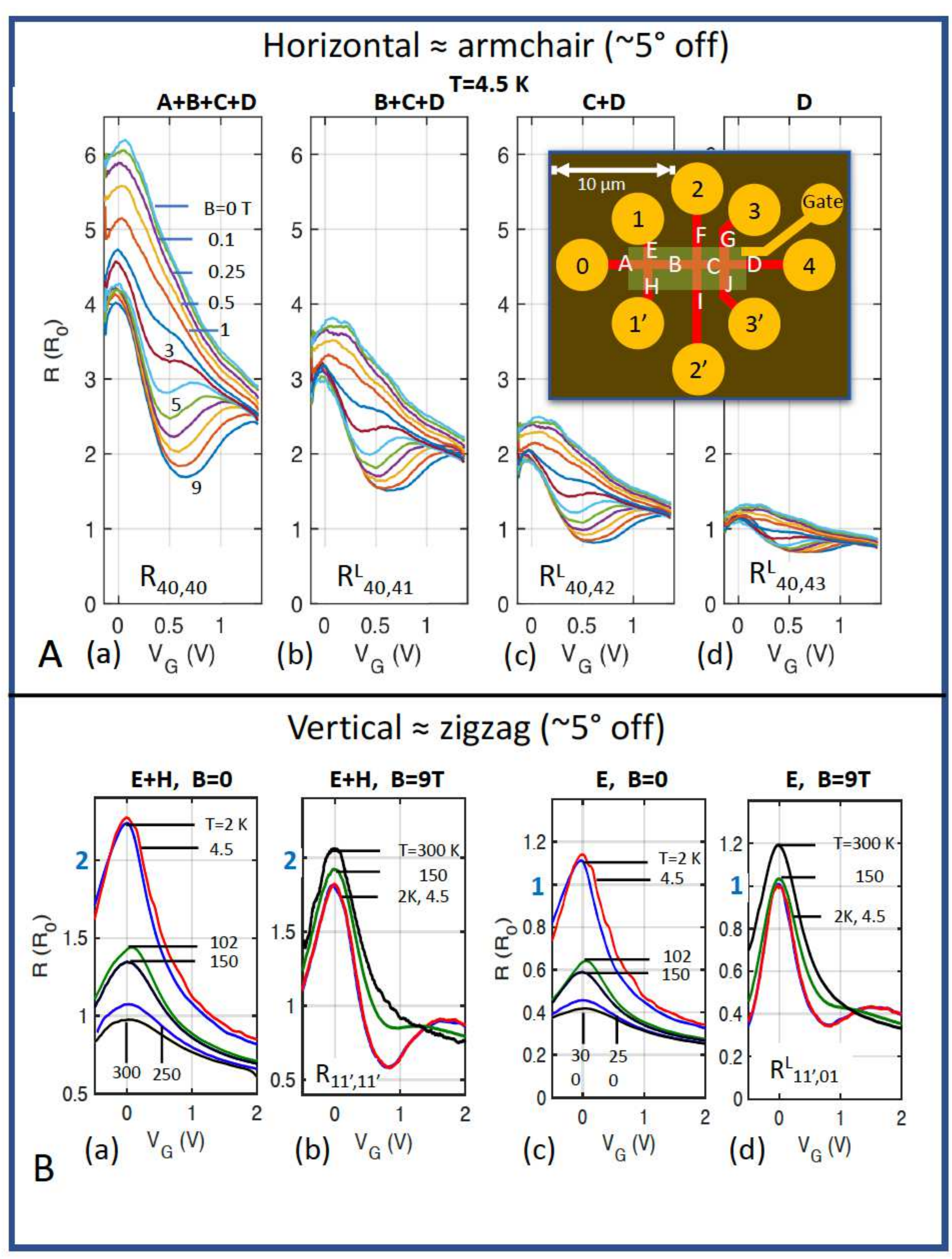

Figure 4. *Quantization and segmentation of the EGES.*

Inset shows the device composed of a 15 µm long 700 nm wide horizontal ribbon crossed with 3 vertical ribbons giving 10 segments (white letters), 3 junctions, 8 low resistance Ohmic Pd-Au contacts. Measured segment lengths, in µm: L_A=3.6; L_B=3.3; L_C=1.7; L_D=4.5; L_E=1.6; L_F=4.0; L_G=3.3; L_H=3.6; L_I=6.8; L_J=3.8; (see Fig. S4). Vertical is 5° from the zigzag edge direction. The nominal gate efficiency (shaded rectangle) is dn_c/dV_G=-0.9x10^{12} V^{-1}cm^{-2} (see Fig. S5). For the ungated sections, $n_c \approx$-1x10^{12} /cm^2. Gate voltages V_G are reported with respect to CNP. (**A**) *Horizontal segmentation*. $R^L_{40,4X}$ (X=0, 1, 2, 3) of the horizontal segments **A**, **B**, **C**, **D** (T=4.5 K, |B| from 0 to 9 T and V_G from -0.1 to 1.3 V). At CNP and |B|≥2 T, $R^L_{40,4X}$ = 4, 3, 2, 1 R_0 for X=0, 1, 2, 3, demonstrating 1 G_0 conductance quantization of the EGES in the segments, and scattering at the junctions. At CNP and |B|≤2 T resistance increases are caused by weak localization at the junctions (see also Fig. 6B). At V_G≈0.5 V, B>2 T large resistance dips are bulk related Shubnikov de Haas oscillations (see also Fig. 6A). (**B**) *Vertical segmentation*. **(a) (b)** segments **E+H** ($R_{11',11'}$); **(c) (d)** segment **E** ($R^L_{11',01}$). For **(a) (c)** B=0 T: resistance reduction at CNP with increasing temperature is due to thermal population of the bulk subbands (see Fig. 5B). **(b) (d)** B=9 T: EGES resistance quantization at CNP is observed up to T=300 K.

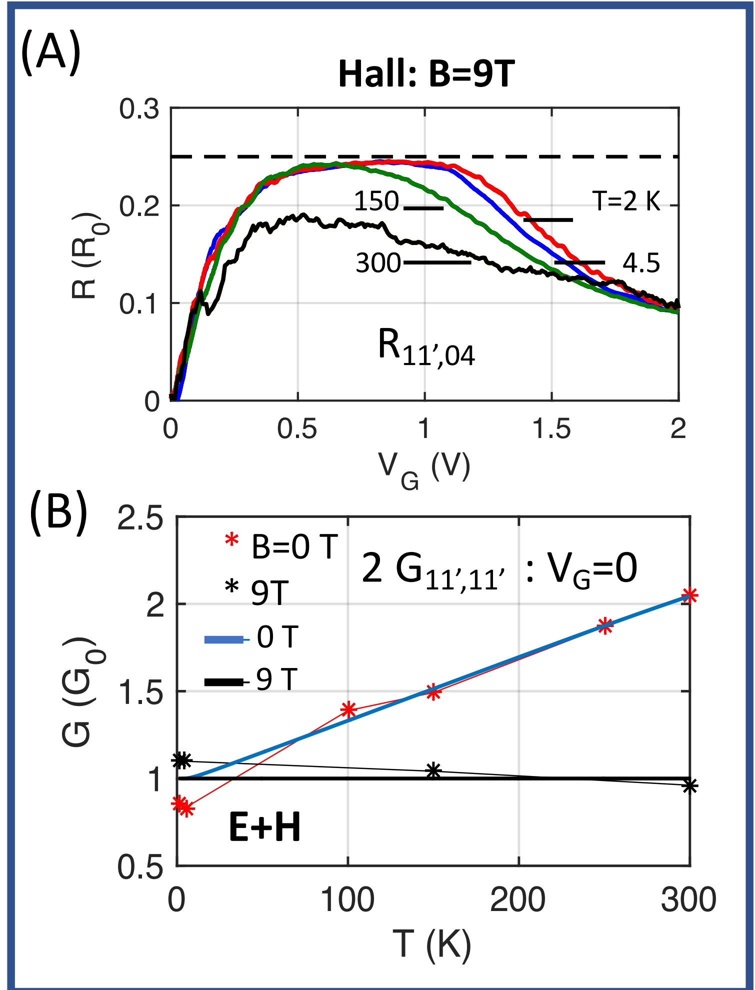

Figure 5. *High temperature measurements.*

(**A**) Hall resistance $R_{11',04}$ at B=9 T, for temperatures T from 2 K to 300 K. The Hall plateau R_{Hall}≈0.25 R_0 observed up to T=150 K corresponds to the Shubnikov-de Haas resistance dips at B=9 T. (**B**) (Red stars) 2x$G_{11',11'}$ as a function of temperature at V_G=0; the factor 2 accounts for segments **E** and **H** in series. For B=0 T and temperatures T>100 K, the conductance at CNP increases due to thermal broadening of the bulk states near CNP, consistent with Eq. 1 (bold blue line). (Note that this increase is not seen in 2D N-EG nor in the 40 nm wide self-assembled ribbons[26], see Fig. S2). (Black stars) For B=9 T the conductance is approximately constant and quantized at 1 G_0 (black line), consistent with Eq. 1.

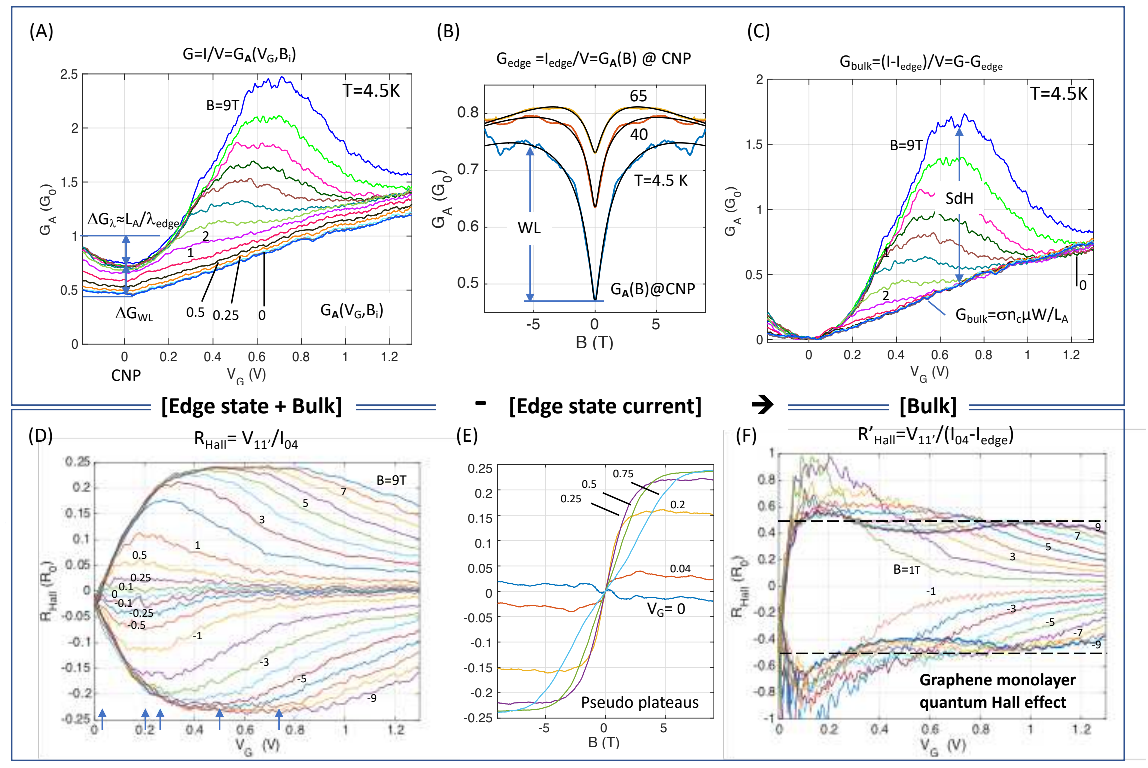

Figure 6 *Independence of the EGES, pinning at E=0, and absence of a EGES Hall voltage*

(**A**) Longitudinal conductance of Segment **A**: $G^{L}_{04,01}(V_G, B_i)=1/R^{L}_{04,01}(V_G, B_i)$ at T=4.5 K for various $|B_i|$. (**B**) The EGES conductance of Segment **A** measured at CNP: $G^{L}_{04,01}(B, V_G=0)$ for T=4.5, 40, 65 K. Weak localization causes conductance dips; (black lines) fits from weak localization theory.[66] (**C**) Subtraction of the (EGES) current measured at CNP (i.e. $I_{edge}=I(B, V_G=0)$) from conductance of Segment **A** reveals diffusive bulk graphene properties (μ=750 cm^2/Vs): for small B, linear conductance; for large B, a SdH conductance peak (corresponding to the resistance dip in Figs. 4A, 4B). Since subtracting the EGES conductivity measured at CNP recovers bulk properties for all V_G, the EGES conductivity is independent of V_G, consistent with pinning at E=0 (See Fig. S8 for T=40 K and 65 K). (**D**) Hall resistance R_{Hall} of the **A-B** junction, T=4.5 K. Note the anomalous pseudo Hall plateaus at ≈ 0.24 G_0 and the B-independent R_{Hall} increase near CNP. (**E**) Corresponding pseudo-plateaus in the magnetic field sweeps $G(V_{Gi},B)$ measured at representative V_{Gi} indicated by arrows in (**D**). (**F**) Subtracting I_{edge}

from the total current reveals the expected graphene quantum Hall plateaus at $R'_{Hall} = \pm 0.5\ R_0$. Hence the EGES produces a V_G-independent, B- dependent current that adds to the bulk current without contributing to the Hall voltage. Summarizing: (1) Only the EGES (not the bulk) contributes to $G(V_G=0, B)$; (2) Subtracting $I(V_G=0, B)$ produces $G_{bulk}(V_G, B)$, hence the EGES is pinned at CNP and the EGES current is independent of the bulk current; (3) The EGES current does not contribute to R_{Hall} (B, V_G); (5) Weak localization of the EGES at the junctions causes T and B dependence of G(T, B, V_G) at all V_G for small B. Hence, we now identify the EGES with the edge-localized branch of the n=0 subband, and the bulk with the delocalized subbands (including the delocalized branch of the n=0 subband), Fig. 1C, which explains the pinning of the EGES; the wave function overlap of these two components is negligible (possibly also in a magnetic field) therefore the EGES is decoupled from the bulk.

References

1 Geim, A. K. & Novoselov, K. S. The rise of graphene. *Nature Materials* **6**, 183 (2007).

2 Han, M. Y., Brant, J. C. & Kim, P. Electron Transport in Disordered Graphene Nanoribbons. *Physical Review Letters* **104**, 056801 (2010).

3 Stampfer, C. *et al.* Energy Gaps in Etched Graphene Nanoribbons. *Physical Review Letters* **102**, 056403 (2009).

4 Gallagher, P., Todd, K. & Goldhaber-Gordon, D. Disorder-induced gap behavior in graphene nanoribbons. *Physical Review B* **81**, 115409 (2010).

5 Epping, A. *et al.* Insulating State in Low-Disorder Graphene Nanoribbons. *physica status solidi (b)* **256**, 1900269 (2019).

6 Marguerite, A. *et al.* Imaging work and dissipation in the quantum Hall state in graphene. *Nature* **575**, 628-633 (2019).

7 Fujita, M., Wakabayashi, K., Nakada, K. & Kusakabe, K. Peculiar localized state at zigzag graphite edge. *J Phys Soc Jpn* **65**, 1920-1923 (1996).

8 Nakada, K., Fujita, M., Dresselhaus, G. & Dresselhaus, M. S. Edge state in graphene ribbons: Nanometer size effect and edge shape dependence. *Physical Review B* **54**, 17954-17961 (1996).

9 Wakabayashi, K., Takane, Y. & Sigrist, M. Perfectly conducting channel and universality crossover in disordered graphene nanoribbons. *Physical Review Letters* **99**, 036601 (2007).

10 Areshkin, D. A., Gunlycke, D. & White, C. T. Ballistic transport in graphene nanostrips in the presence of disorder: Importance of edge effects. *Nano Lett* **7**, 204-210 (2007).

11 Gunlycke, D., Lawler, H. M. & White, C. T. Room-temperature ballistic transport in narrow graphene strips. *Physical Review B* **75**, 085418 (2007).

12 Akhmerov, A. R. & Beenakker, C. W. J. Boundary conditions for Dirac fermions on a terminated honeycomb lattice. *Physical Review B* **77**, 085423 (2008).

13 Das Sarma, S., Adam, S., Hwang, E. H. & Rossi, E. Electronic Transport in Two-Dimensional Graphene. *Review of Modern Physics* **83**, 407-466 (2011).

14 Castro Neto, A. H., Guinea, F., Peres, N. M. R., Novoselov, K. S. & Geim, A. K. The electronic properties of graphene. *Rev Mod Phys* **81**, 109-162 (2009).

15 Brey, L. & Fertig, H. A. Electronic states of graphene nanoribbons studied with the Dirac equation. *Physical Review B* **73**, 235411 (2006).

16 Lin, L., Peng, H. & Liu, Z. Synthesis challenges for graphene industry. *Nature Materials* **18**, 520-524 (2019).

17 Neumaier, D., Pindl, S. & Lemme, M. C. Integrating graphene into semiconductor fabrication lines. *Nature Materials* **18**, 525-529 (2019).

18 Abanin, D. A., Lee, P. A. & Levitov, L. S. Spin-Filtered Edge States and Quantum Hall Effect in Graphene. *Physical Review Letters* **96**, 176803 (2006).

19 Zhang, Y. B., Tan, Y. W., Stormer, H. L. & Kim, P. Experimental observation of the quantum Hall effect and Berry's phase in graphene. *Nature* **438**, 201 (2005).

20 Novoselov, K. S. *et al.* Two-dimensional gas of massless Dirac fermions in graphene. *Nature* **438**, 197-200 (2005).

21 Goerbig, M. O. Electronic properties of graphene in a strong magnetic field. *Rev Mod Phys* **83**, 1193-1243 (2011).

22 Young, A. F. *et al.* Tunable symmetry breaking and helical edge transport in a graphene quantum spin Hall state. *Nature* **505**, 528-532 (2014).

23 Veyrat, L. *et al.* Helical quantum Hall phase in graphene on SrTiO3. *Science* **367**, 781-786 (2020).

24 Brey, L. & Fertig, H. A. Edge states and the quantized Hall effect in graphene. *Physical Review B* **73**, 195408 (2006).

25 Sprinkle, M. *et al.* Scalable templated growth of graphene nanoribbons on SiC. *Nat Nanotechnol* **5**, 727-731 (2010).

26 Baringhaus, J. *et al.* Exceptional ballistic transport in epitaxial graphene nanoribbons. *Nature* **506**, 349-354 (2014).

27 Ruan, M. *Structured epitaxial graphene for electronics* PhD thesis, PhD - Georgia Institute of Technology, (2012).

28 Palacio, I. *et al.* Atomic Structure of Epitaxial Graphene Sidewall Nanoribbons: Flat Graphene, Miniribbons, and the Confinement Gap. *Nano Lett* **15**, 182−189 (2015).

29 Norimatsu, W. & Kusunoki, M. Growth of graphene from SiC{0001} surfaces and its mechanisms. *Semicond Sci Tech* **29**, 064009 (2014).

30 Baringhaus, J., Edler, F. & Tegenkamp, C. Edge-states in graphene nanoribbons: a combined spectroscopy and transport study. *Journal of Physics-Condensed Matter* **25**, 392001(392005pp) (2013).

31 Lado, J. L., Garcia-Martinez, N. & Fernandez-Rossier, J. Edge states in graphene-like systems. *Synthetic Met* **210**, 56-67 (2015).

32 Berger, C. *et al.* Electronic confinement and coherence in patterned epitaxial graphene. *Science* **312**, 1191-1196 (2006).

33 Ohta, T. *et al.* Interlayer interaction and electronic screening in multilayer graphene investigated with angle-resolved photoemission spectroscopy. *Physical Review Letters* **98**, 206802 (2007).

34 Berger, C., Conrad, E. & de Heer, W. A. in *Physics of Solid Surfaces, Landolt Börstein encyclopedia* Vol. Subvolume B *Physics of Solid Surfaces* (ed P. Chiaradia G. Chiarotti) Ch. 164-171, 727-807. ArXiv:1704.00374 (Springer-Verlag, 2018).

35 Wu, X. S. *et al.* Half integer quantum Hall effect in high mobility single layer epitaxial graphene. *Appl Phys Lett* **95**, 223108 (2009).

36 Tzalenchuk, A. *et al.* Towards a quantum resistance standard based on epitaxial graphene. *Nat Nanotechnol* **5**, 186-189 (2010).

37 San-Jose, P., Lado, J. L., Aguado, R., Guinea, F. & Fernandez-Rossier, J. Majorana Zero Modes in Graphene. *Physical Review X* **5**, 041042 (2015).

38 de Heer, W. A., Berger, C. & First, P. N. Patterned thin films graphite devices and methods for making the same. *US patent US7015142B2 (Provisional filed Jun. 12, 2003; granted March 3, 2006); European patent EP1636829B. This patent, based on experimental evidence, includes a detailed description of practical epitaxial graphene coherent nanoelectronics.*

39 Wakabayashi, K. Electronic transport properties of nanographite ribbon junctions. *Physical Review B* **64**, 125428 (2001).

40 Tao, C. G. *et al.* Spatially resolving edge states of chiral graphene nanoribbons. *Nature Physics* **7**, 616-620 (2011).

41 Rizzo, D. J. *et al.* Inducing metallicity in graphene nanoribbons via zero-mode superlattices. *Science* **369**, 1597-1603 (2020).

42 Plasser, F. *et al.* The Multiradical Character of One- and Two-Dimensional Graphene Nanoribbons. *Angew Chem Int Edit* **52**, 2581-2584 (2013).

43 Sun, Z. & Wu, J. S. Open-shell polycyclic aromatic hydrocarbons. *J Mater Chem* **22**, 4151-4160 (2012).

44 Stein, S. E. & Brown, R. L. Pi-Electron Properties of Large Condensed Polyaromatic Hydrocarbons. *J Am Chem Soc* **109**, 3721-3729 (1987).

45 Guo, J., Yoon, Y. & Ouyang, Y. Gate Electrostatics and Quantum Capacitance of Graphene Nanoribbons. *Nano Lett* **7**, 1935-1940 (2007).

46 Ashcroft, N. W. & Mermin, N. D. Solid State Physics. *HRW International Editions* (1988).

47 Kane, C. L. & Mele, E. J. Quantum spin Hall effect in graphene. *Physical Review Letters* **95**, 226801 (2005).

48 Li, J., Niquet, Y.-M. & Delerue, C. Magnetic-Phase Dependence of the Spin Carrier Mean Free Path in Graphene Nanoribbons. *Physical Review Letters* **116**, 236602 (2016).

49 Fertig, H. A. & Brey, L. Luttinger liquid at the edge of undoped graphene in a strong magnetic field. *Physical Review Letters* **97**, 116805 (2006).

50 Yazyev, O. V., Capaz, R. B. & Louie, S. G. Theory of magnetic edge states in chiral graphene nanoribbons. *Physical Review B* **84**, 115406(115405pp) (2011).

51 Ryu, S. & Hatsugai, Y. Topological Origin of Zero-Energy Edge States in Particle-Hole Symmetric Systems. *Physical Review Letters* **89**, 077002 (2002).

52 Ristein, J., Mammadov, S. & Seyller, T. Origin of Doping in Quasi-Free-Standing Graphene on Silicon Carbide. *Physical Review Letters* **108**, 246104 (2012).

53 Berger, C. *et al.* Ultrathin Epitaxial Graphite: 2D Electron Gas Properties And a Route Toward Graphene-Based Nanoelectronics. *J Phys Chem B* **108**, 19912-19916 (2004).

54 Van Bommel, A. J., Crobeen, J. E. & Van Tooren, A. LEED and Auger electron observations of the SiC(0001) surface. *Surface Science* **48**, 463-472 (1975).

55 de Heer, W. A. *et al.* Large Area and Structured Epitaxial Graphene Produced by Confinement Controlled Sublimation of Silicon Carbide. *Proc Nat Acad Sci* **108**, 16900-16905 (2011).

56 Hicks, J. *et al.* A wide-bandgap metal-semiconductor-metal nanostructure made entirely from graphene. *Nature Physics* **9**, 49-54 (2013).

57 De Cecco, A. *et al.* Non-Invasive Nanoscale Potentiometry and Ballistic Transport in Epigraphene Nanoribbons. *Nano Lett* **20**, 3786-3790 (2020).

58 Wei, Z. Q. *et al.* Nanoscale Tunable Reduction of Graphene Oxide for Graphene Electronics. *Science* **328**, 1373-1376 (2010).

59 Wu, X. S. *et al.* Epitaxial-graphene/graphene-oxide junction: An essential step towards epitaxial graphene electronics. *Physical Review Letters* **101**, 026801 (2008).

60 Cardinaud, C., Peignon, M.-C. & Tessier, P.-Y. Plasma etching: principles, mechanisms, application to micro- and nano-technologies. *Applied Surface Science* **164**, 72-83 (2000).

61 Ito, H. *et al.* Tight-binding quantum chemical molecular dynamics simulations for the elucidation of chemical reaction dynamics in SiC etching with SF6/O2 plasma. *Phys Chem Chem Phys* **18**, 7808-7819 (2016).

62 Datta, S. *Electronic transport in mesoscopic systems*. (Cambridge University Press, 1995).

63 Chen, J. H. *et al.* Charged-impurity scattering in graphene. *Nature Physics* **4**, 377-381 (2008).

64 Rengel, R., Pascual, E. & Martín, M. J. Influence of the substrate on the diffusion coefficient and the momentum relaxation in graphene: The role of surface polar phonons. *Appl Phys Lett* **104**, 233107 (2014).

65 Beenakker, C. W. J. & Vanhouten, H. Quantum Transport in Semiconductor Nanostructures. *Solid State Phys* **44**, 1-228 (1991).

66 McCann, E. *et al.* Weak-localization magnetoresistance and valley symmetry in graphene. *Physical Review Letters* **97**, 146805 (2006).

67 Eless, V. *et al.* Phase coherence and energy relaxation in epitaxial graphene under microwave radiation. *Appl Phys Lett* **103**, 093103 (2013).

68 Lifshitz, I. M. & Kosevich, A. M. Theory of Magnetic Susceptibility in Metals at Low Temperatures. *Soviet Physics JETP* **2**, 636 (1955).

69 Tan, Y. W. *et al.* Measurement of scattering rate and minimum conductivity in graphene. *Physical Review Letters* **99**, 246803 (2007).

70 Novoselov, K. S. *et al.* Two-dimensional gas of massless Dirac fermions in graphene. *Nature* **438**, 197 (2005).

71 Ribeiro-Palau, R. *et al.* Quantum Hall resistance standard in graphene devices under relaxed experimental conditions. *Nat Nanotechnol* **10**, 965-U168 (2015).

72 Massabeau, S. *et al.* Evidence of Fermi level pinning at the Dirac point in epitaxial multilayer graphene. *Physical Review B* **95**, 085311 (2017).

73 Wang, L. *et al.* Tuning magnetotransport in a compensated semimetal at the atomic scale. *Nat Commun* **6**, 8892 (2015).

74 Curtin, A. E. *et al.* Kelvin probe microscopy and electronic transport in graphene on SiC(0001) in the minimum conductivity regime. *Appl Phys Lett* **98**, 243111 (2011).

75 Ferrari, A. C. *et al.* Raman spectrum of graphene and graphene layers. *Physical Review Letters* **97**, 187401 (2006).

Figures

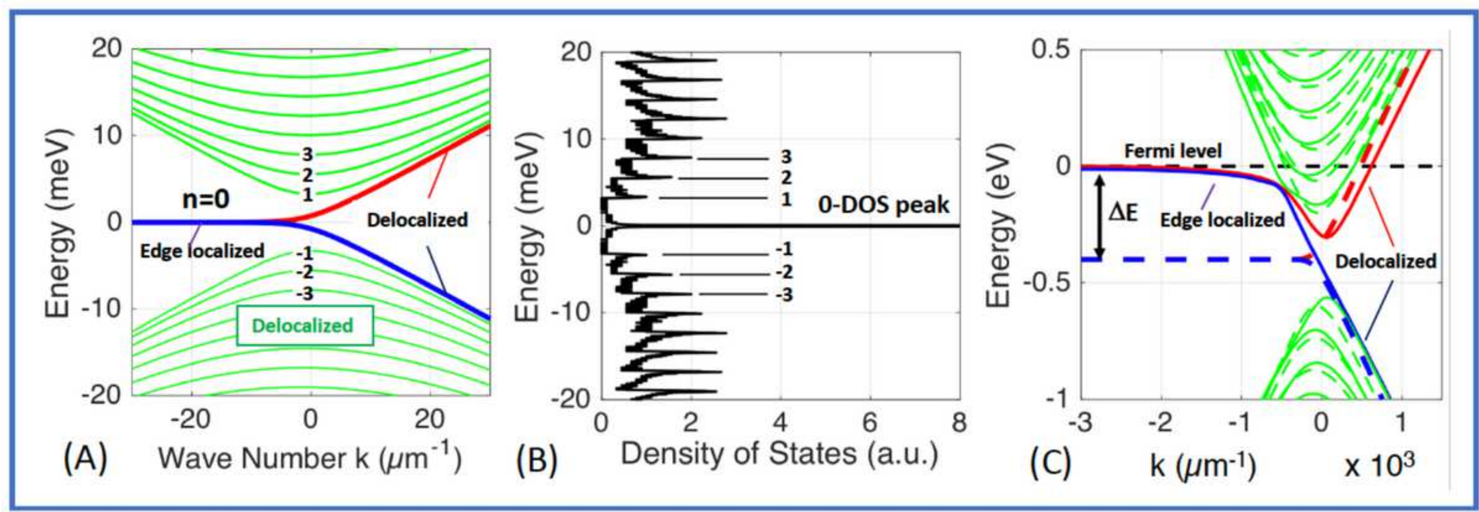

Figure 1

Electronic structure of graphene ribbons. Please see manuscript .pdf for full caption.

Figure 2

Neutral epigraphene characterization. Please see manuscript .pdf for full caption.

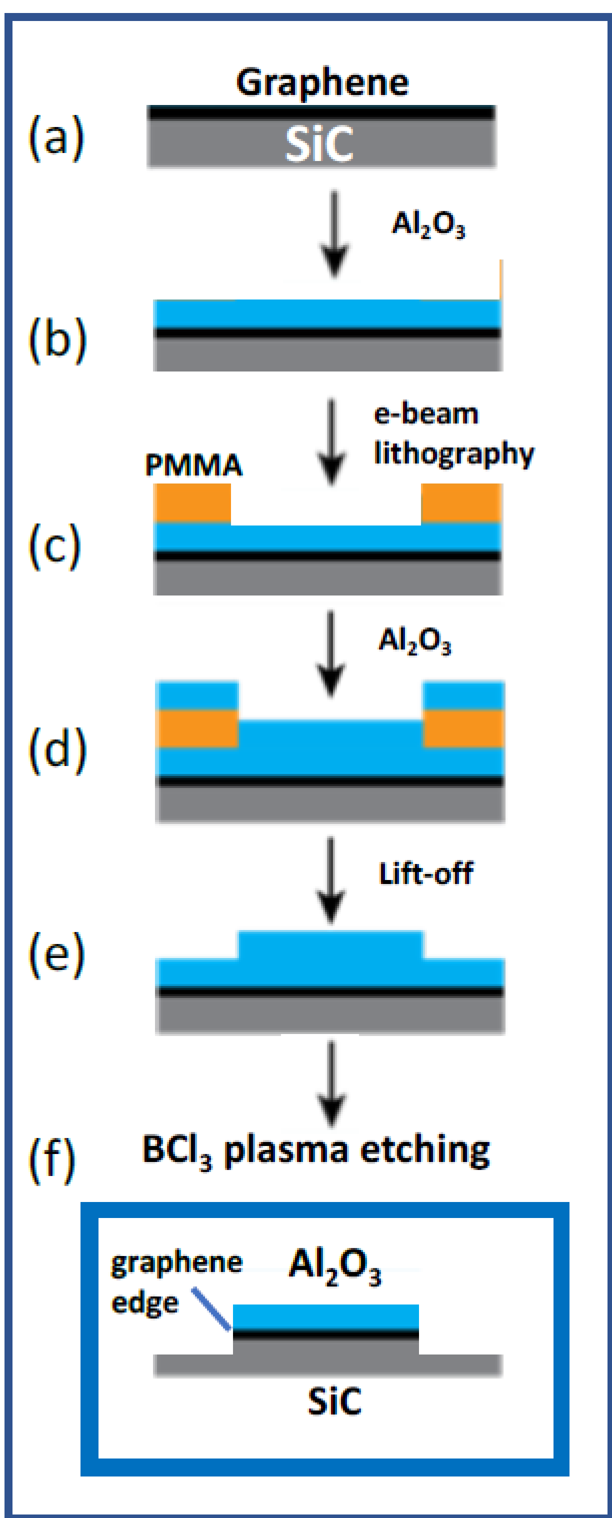

Figure 3

Nanolithography process that ensures the integrity of the graphene edges. (a) High temperature annealing of N-EG at 1500°C preferentially evaporates silicon and the remaining carbon rich surface anneals to produce a high quality epigraphene monolayer.55 (b) A 30 nm alumina layer is deposited, securely embedding the graphene between alumina and silicon carbide. (c) After development of e-beam patterned polymer mask. (d) Application of 20 nm of alumina. (e) After lift off the polymer mask. (f) A

highly directional plasma (ICP) uniformly cuts through the alumina/graphene/SiC sandwich and 16 nm into the SiC. The high temperature (>5000°C) in the plasma vaporizes all of the materials in the sandwich and is expected to fuse the graphene edges to the SiC61.

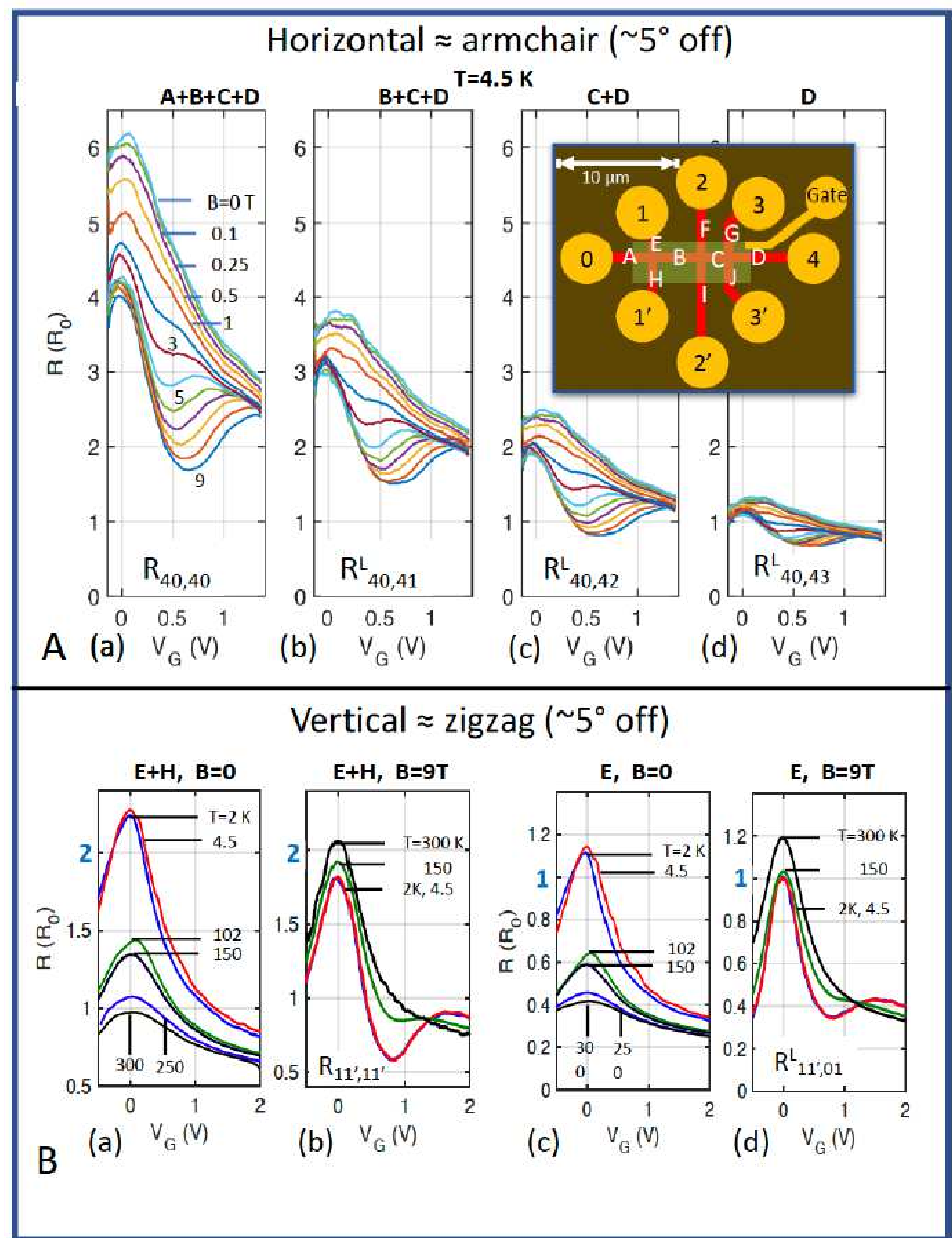

Figure 4

Quantization and segmentation of the EGES. Inset shows the device composed of a 15 μm long 700 nm wide horizontal ribbon crossed with 3 vertical ribbons giving 10 segments (white letters), 3 junctions, 8

low resistance Ohmic Pd-Au contacts. Measured segment lengths, in µm: LA=3.6; LB=3.3; LC=1.7; LD=4.5; LE=1.6; LF=4.0; LG=3.3; LH=3.6; LI=6.8; LJ=3.8; (see Fig. S4). Vertical is 5° from the zigzag edge direction. The nominal gate efficiency (shaded rectangle) is dnc/dVG=-0.9x1012 V-1cm-2 (see Fig. S5). For the ungated sections, nc ≈-1x1012 /cm2. Gate voltages VG are reported with respect to CNP. (A) Horizontal segmentation. RL40,4X (X=0, 1, 2, 3) of the horizontal segments A, B, C, D (T=4.5 K, |B| from 0 to 9 T and VG from -0.1 to 1.3 V). At CNP and |B|≥2 T, RL40,4X = 4, 3, 2, 1 R0 for X=0, 1, 2, 3, demonstrating 1 G0 conductance quantization of the EGES in the segments, and scattering at the junctions. At CNP and |B|≤2 T resistance increases are caused by weak localization at the junctions (see also Fig. 6B). At VG≈0.5 V, B>2 T large resistance dips are bulk related Shubnikov de Haas oscillations (see also Fig. 6A). (B) Vertical segmentation. (a) (b) segments E+H (R11',11'); (c) (d) segment E (RL11',01). For (a) (c) B=0 T: resistance reduction at CNP with increasing temperature is due to thermal population of the bulk subbands (see Fig. 5B). (b) (d) B=9 T: EGES resistance quantization at CNP is observed up to T=300 K.

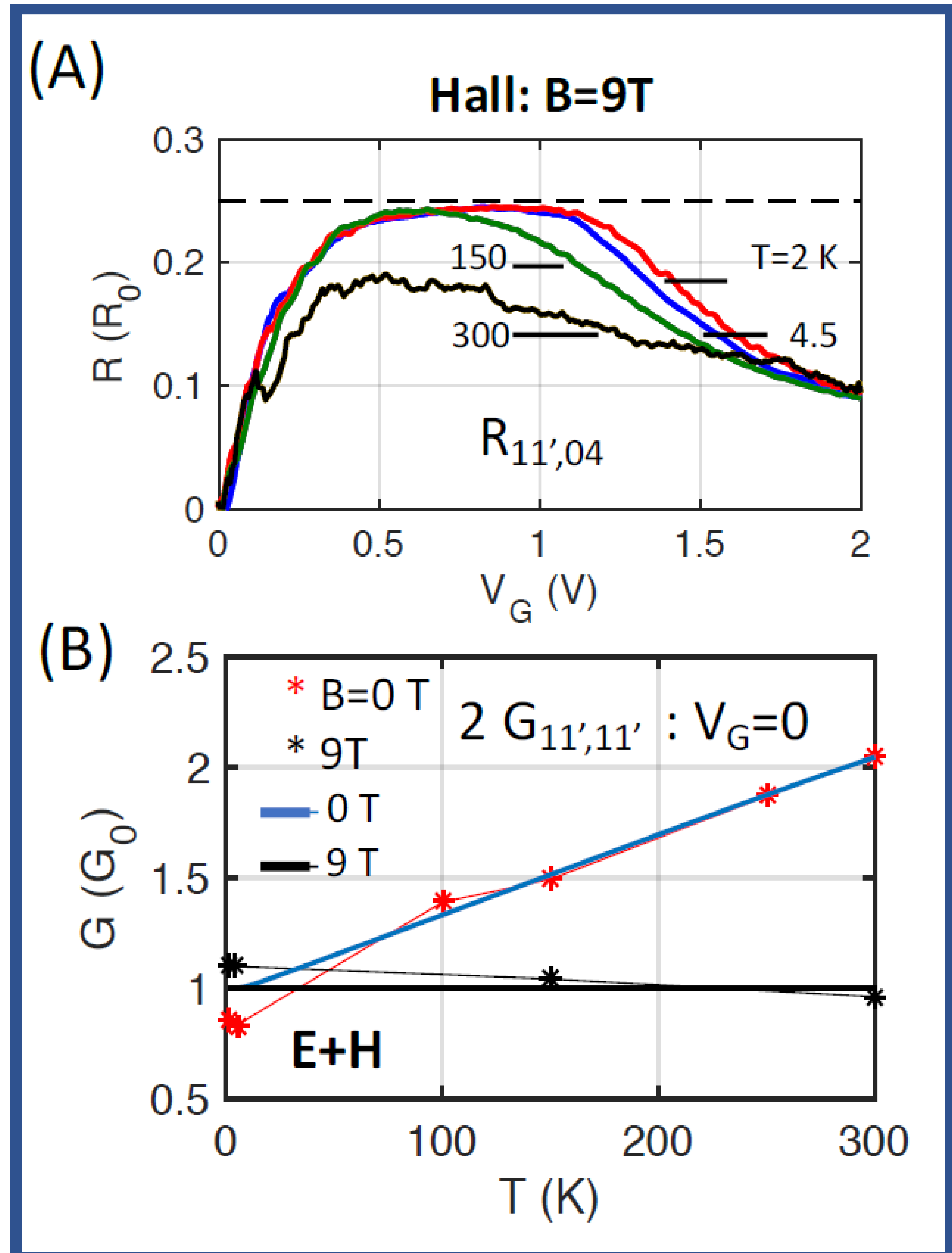

Figure 5

High temperature measurements. (A) Hall resistance R11',04 at B=9 T, for temperatures T from 2 K to 300 K. The Hall plateau RHall≈0.25 R0 observed up to T=150 K corresponds to the Shubnikov-de Haas resistance dips at B=9 T. (B) (Red stars) 2xG11',11' as a function of temperature at VG=0; the factor 2 accounts for segments E and H in series. For B=0 T and temperatures T>100 K, the conductance at CNP increases due to thermal broadening of the bulk states near CNP, consistent with Eq. 1 (bold blue line).

(Note that this increase is not seen in 2D N-EG nor in the 40 nm wide self-assembled ribbons26, see Fig. S2). (Black stars) For B=9 T the conductance is approximately constant and quantized at 1 G0 (black line), consistent with Eq. 1.

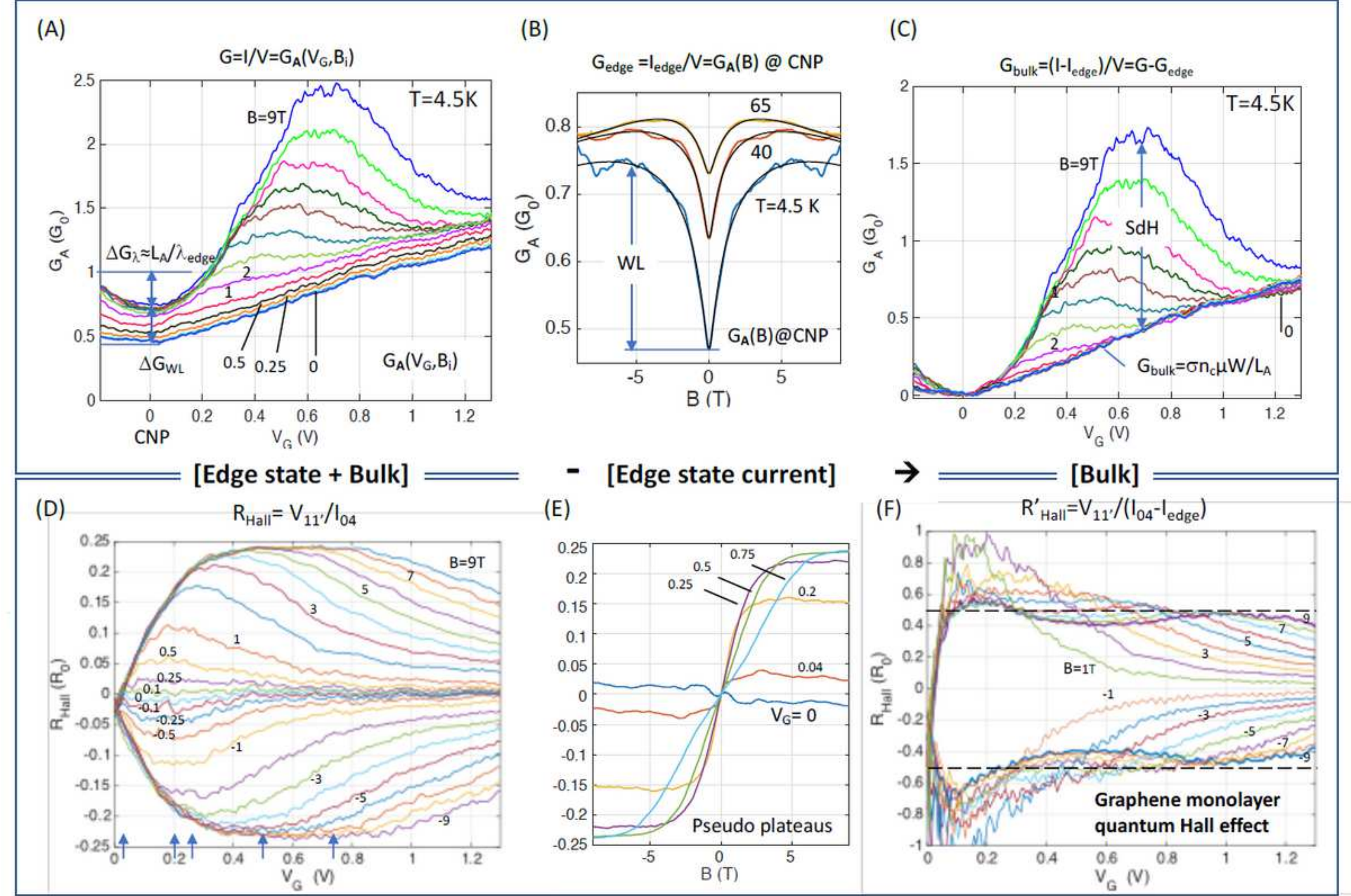

Figure 6

Independence of the EGES, pinning at E=0, and absence of a EGES Hall voltage. Please see manuscript .pdf for full caption.

Supplementary Files

This is a list of supplementary files associated with this preprint. Click to download.

- PrudkovskiyEdgeStateSupp.pdf